Analysis of Turbulence Collapse in the Stably Stratified Surface Layer Using Direct Numerical Simulation

Boundary-Layer Meteorology
An International Journal
of Physical, Chemical and
Biological Processes in the
Atmospheric Boundary Layer

ISSN 0006-8314
Volume 139
Number 2

Boundary-Layer Meteorol
(2011) 139:241-259
DOI 10.1007/
s10546-011-9588-2

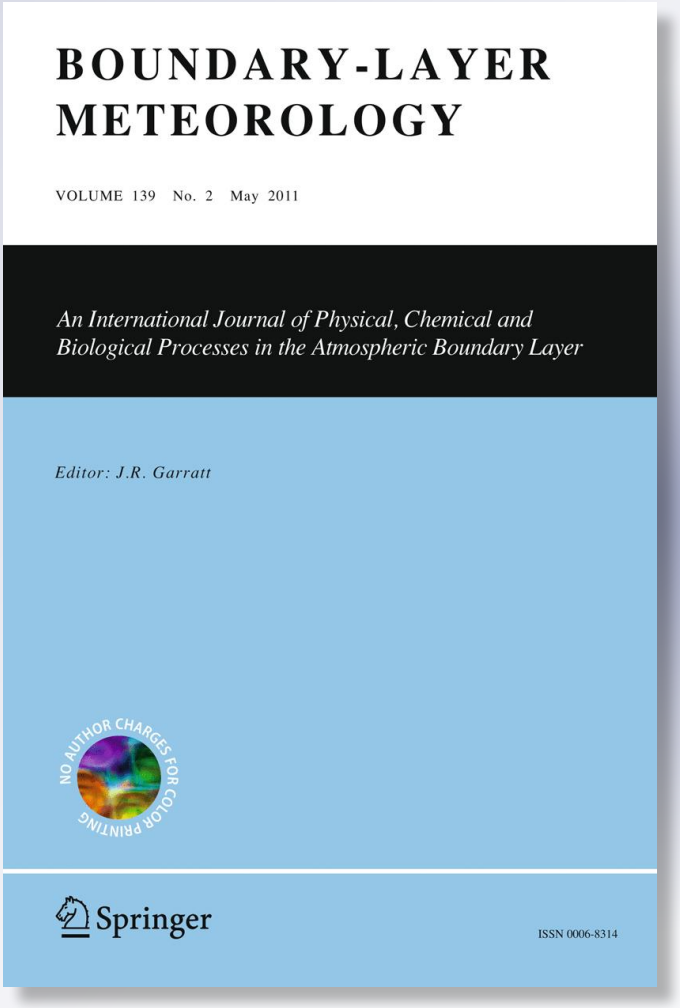

Springer

Boundary-Layer Meteorol (2011) 139:241–259
DOI 10.1007/s10546-011-9588-2

ARTICLE

Analysis of Turbulence Collapse in the Stably Stratified Surface Layer Using Direct Numerical Simulation

O. Flores · J. J. Riley

Received: 5 May 2010 / Accepted: 4 January 2011 / Published online: 26 January 2011

Abstract The nocturnal atmospheric boundary layer (ABL) poses several challenges to standard turbulence and dispersion models, since the stable stratification imposed by the radiative cooling of the ground modifies the flow turbulence in ways that are not yet completely understood. In the present work we perform direct numerical simulation of a turbulent open channel flow with a constant (cooling) heat flux imposed at the ground. This configuration provides a very simplified model for the surface layer at night. As a result of the ground cooling, the Reynolds stresses and the turbulent fluctuations near the ground re-adjust on times of the order of L/u_τ, where L is the Obukhov length scale and u_τ is the friction velocity. For relatively weak cooling turbulence survives, but when $Re_L = Lu_\tau/\nu \lesssim 100$ turbulence collapses, a situation that is also observed in the ABL. This criterion, which can be locally measured in the field, is justified in terms of the scale separation between the largest and smallest structures of the dynamic sublayer.

Keywords Intermittent turbulence · Obukhov length · Nocturnal boundary layer · Numerical simulation · Stable surface layer · Turbulence collapse

1 Introduction

The nocturnal atmospheric boundary layer has received considerable attention during the past years, mainly because it is one of the least understood and most difficult aspects to model in the atmospheric boundary layer (ABL). At nighttime the Earth's surface loses heat by radiation, cooling the air in the ABL. The resulting boundary layer becomes stably stratified and, depending on the intensity of the radiative cooling, the turbulent motions can be severely affected.

According to Mahrt (1998), the nocturnal ABL can be classified as weakly stable and very stable. The former is well described by the Monin–Obukhov similarity theory

O. Flores (✉) · J. J. Riley
Department of Mechanical Engineering, University of Washington, Seattle, WA, USA
e-mail: oflores@u.washington.edu

(Monin 1970), since turbulence is more or less continuous and quasi-steady. On the other hand, the very stable case is more complex, with periods of relatively weak or unmeasurable fluctuations followed by turbulent events (global intermittency, as defined by Mahrt). The very stable case is also very important from a practical point of view, since the reduced turbulence can lead to strong concentrations of contaminants, and the reduced downward heat flux can result in very low surface temperatures and eventual frost damage. It is also not clear whether the stratification can be strong enough to produce a collapse of the turbulence, resulting in the runaway cooling predicted by Reynolds-averaged Navier-Stokes (RANS) simulations (Derbyshire 1999; Van de Wiel et al. 2007).

It is important to note that, while the weakly stable case is well suited for large-eddy simulation (LES), e.g. Saiki et al. (2000), Kosovic and Curry (2000) and Beare et al. (2006), the very stable case remains elusive for LES models (Mahrt 1998). First, the reduction of the size of the characteristic eddies is more demanding for subgrid-scale modelling. Second, turbulence may become spatially intermittent, a phenomenon that LES models with horizontal averaging do not support well (Stoll and Porte-Agel 2008).

The structure and scaling of the different layers of the stable ABL are described by Monin (1970). The inner part of the nocturnal ABL, where the effects of rotation are negligible, is the surface layer, with thickness typically of the order of tens of metres. Within the surface layer there is a region where stratification effects are small, the dynamic sublayer, whose thickness scales with the Obukhov length scale L. In principle, the dynamic sublayer should resemble the structure of non-stratified wall-bounded turbulence, e.g. as described in Pope (2000). The characteristic velocity scale inside the entire dynamic sublayer is the friction velocity u_τ, while the characteristic length scale varies with the height above the ground. Very close to the ground we have the buffer region when the ground surface is smooth, or the roughness sublayer otherwise. The characteristic length scale in the buffer region is the viscous length scale ν/u_τ, and its height is approximately $100\nu/u_\tau$. The characteristic length scale in the roughness sublayer is the height of the roughness elements k_r, or any equivalent length scale. Typically, the roughness sublayer extends up to $z/k_r \sim 1{-}3$ (Raupach et al. 1991). For the part of the dynamic sublayer where $\nu/u_\tau \ll z \ll L$ (or $k_r \ll z \ll L$), the only possible length scale is z, the distance to the ground itself, yielding a logarithmic mean velocity profile. Above the dynamic sublayer, when $z \gtrsim L$, the Obukhov length scale becomes important, and the similarity theory predicts a 'logarithmic plus linear' mean velocity profile. Note that, as the ground cooling increases, L decreases, resulting in a relatively shallow dynamic sublayer for a strongly stratified ABL.

In order to study the very stable stratified surface layer, Nieuwstadt (2005) performed direct numerical simulations (DNS) of an open turbulent channel flow with stable stratification. This configuration provides a simple model to study the surface layer, where the effects of rotation are negligible (Monin 1970). His simulations were run at relatively low Reynolds numbers, $Re = u_* h/\nu = 360$, where h is the height of the channel and $u_* = (-h\partial_x P/\rho_0)^{1/2}$ is the friction velocity, defined in terms of the streamwise pressure gradient driving the flow, $\partial_x P$. He observed that, during the transient in which an initially non-stratified flow adjusts to the imposed ground cooling, turbulence collapsed when $h/L > 0.51$.[1]

Using numerical simulations of turbulent channel flows at $Re = 180$ with isothermal walls and stable stratification, Garg et al. (2000) and Armenio and Sarkar (2002) observed transient relaminarization of the flow when $Ri_\tau > 45{-}60$, where $Ri_\tau = \Delta\rho g h/\rho_0 u_\tau^2$ is

[1] In Nieuwstadt (2005) L is defined as $L^{(N)} = [u_*^3\rho_0]/[g(w\rho)_0]$, which differs from the Obukhov length scale (see Eq. 9) by a factor of $1/\kappa$, with $\kappa \approx 0.41$ being von Kármán's constant. Here we use L for the Obukhov length scale; thus when Nieuwstadt's results are referenced they are expressed in terms of the Obukhov length scale, $h/L = \kappa h/L^{(N)}$.

the friction Richardson number, defined in terms of the density difference between the walls ($\Delta\rho$) and the friction velocity, u_τ. Expressed in terms of the Obukhov length scale, the critical Ri_τ roughly corresponds to $(h/L)_{crit} \approx 0.24$. This threshold differs from that observed by Nieuwstadt (2005), suggesting a possible Reynolds number dependence. Such a dependence was also predicted by the RANS model of the surface layer developed by Van de Wiel et al. (2007), where $(h/L)_{crit}$ varies from 0.25 to 1.25 when the roughness parameter z_0/h varies between 10^{-1} and 10^{-6}. As pointed out by the authors, $z_0/h \propto Re^{-1}$ for smooth walls, so that the variation of $(h/L)_{crit}$ with z_0/h can be also interpreted as a variation with Re.

Laboratory experiments of the stably stratified turbulent boundary layer performed by Ohya et al. (1997) and Ohya (2001) at higher Reynolds numbers ($Re \approx 1000-4000$) result in higher values for the critical value of h/L at which turbulence collapses. For a smooth surface, turbulent fluctuations are shut down in the lower part of the boundary layer when $h/L \gtrsim 5$ (Ohya et al. 1997). That threshold is reduced to $h/L \gtrsim 2$ when a rough surface is considered (Ohya 2001).

The effect of rotation was neglected in the DNS and laboratory experiments mentioned above, but it was included in the DNS of turbulent Ekman layers performed by Coleman et al. (1992), with Reynolds numbers $Re = u_* \delta/\nu \approx 250$, where $\delta = 0.7 u_*/f$ is the height of the boundary layer. The temperature at the ground was fixed, so that the cooling flux decreased with time, as opposed to the constant heat flux of Nieuwstadt (2005). Interestingly, Coleman et al. (1992) report that, under these conditions, the flow relaminarizes for values of $\delta/L \gtrsim 0.14$.

When the question of turbulence collapse is analyzed using field data with higher Reynolds numbers, the answer seems more elusive. As in the Coleman et al. (1992) simulations, the parameter used in this case is δ/L, where δ is the thickness of the turbulent boundary layer. Using data from the Microfronts experimental campaign (for more details, see Sun 1999), Mahrt (1998) proposed $\delta/L \approx 1$ as the limit between the weakly stable and the very stable regimes, with turbulence collapse and global intermittency being expected in the latter regime. A different value ($\delta/L \approx 0.5$) is proposed in the review of Hogstrom (1996), who considered data from several field experiments. More recently, Van de Wiel et al. (2003) proposed a different parameter to account for turbulence collapse using data from the CASES-99 experimental campaign (Poulos et al. 2002). When CASES-99 data are analyzed in terms of δ/L, intermittency appears at $\delta/L \approx 3-4$, and turbulent heat fluxes are suppressed near the ground ('radiative cooling' cases in the classification of Van de Wiel et al. 2003) for $\delta/L \gtrsim 10^3$. These values are orders of magnitude larger than those reported in numerical simulations and in the laboratory. Part of the disagreement comes from the difference between h and δ. The former is the height of the surface layer, where the effect of rotation is negligible, while δ is the height of the atmospheric boundary layer. However, this difference does not explain the wide range of variation within the nocturnal ABL data, and within the laboratory and simulation data, which suggests that h/L (or δ/L) is not an appropriate parameter to characterize turbulence collapse under strong stratification.

Finally, it is important to realize that there is some inconsistency in the literature around the term 'turbulence collapse'. Sometimes it is used to describe when the flow undergoes partial or total relaminarization during its time evolution, but at other times it is used to describe the final state of the flow (once a statistically steady state has been reached). As pointed out by Armenio and Sarkar (2002), an isothermal channel flow with $Re = 180$ and $Ri_\tau = 60$ undergoes a transition and becomes laminar once a constant temperature difference is imposed between its walls. However, since the channel is driven by a constant pressure gradient in the streamwise direction, the mean velocity increases until the flow becomes unstable, and turbulence is recovered. In the present study, we focus on the transition of a non-stratified

turbulent flow into a stably stratified regime, and 'turbulence collapse' implies that during that transition the flow relaminarizes.

The objective of the present work is to analyze in more detail the collapse of the turbulence under stable stratification, in order to obtain a criterion that is independent of the Re of the flow. To that end, we perform high resolution DNS of turbulent open channel flows with a constant cooling heat flux imposed at the ground. We deliberately choose a simplified scenario, such as that used by Nieuwstadt (2005), where the interactions between turbulence and stratification can be investigated directly. A hydrodynamically smooth ground is used here, since it is known that the effect of roughness is essentially limited to the roughness sublayer, and that flow structures with sizes larger than a few k_r are not directly influenced by the details of the ground (Flores et al. 2007). Radiative heat transfer to the surface and between fluid elements, which are known to have an important role in the very stable ABL (Edwards 2009), are not taken into account. Also, the Coriolis effect due to the Earth rotation is ignored, and in that sense our simulations can be understood as an approximation to the nocturnal surface layer, rather than to the nocturnal ABL. As a consequence, all the turbulence generation in our simulations is associated with ground-based wind shear, and the top-down interactions associated with the presence of low-level jets (LLJ) are not included in our simulations, even though LLJs are a common feature of the nocturnal boundary layer (Cuxart and Jiménez 2007). All those limitations have to be taken into account when comparing our simulations results with measurements in the ABL.

It is worth noting that the present DNS have higher Reynolds numbers that those previously used, allowing us to reduce the gap between simulations and experimental observations. Our Re values are high enough that an incipient logarithmic region exists, which allows the use of the Reynolds number similarity to extrapolate our results to the relatively low Re of the very stable atmospheric surface layer.

The paper is organized as follows. Section 2 describes the details of the numerical code, as well as the parameters used in the different simulations. Section 3 presents the results, starting with the description of the evolution of the flow (Sect. 3.1), followed by a detailed analysis of the collapse of the turbulence (Sect. 3.3) and how it is affected by the large-scale structures in the flow (Sect. 3.4). Conclusions are offered in Sect. 4.

2 Description of the Numerical Simulations

The flow geometry considered in the present study is the same as that used by Nieuwstadt (2005): open channel flow, statistically homogeneous in the horizontal directions, and driven by a constant pressure gradient in the streamwise direction (x). As mentioned in the introduction, rotation and radiative heat transfer in the air are not included in the simulations.

We perform direct numerical simulations (DNS) of the Navier-Stokes equations with the Boussinesq approximation (Spiegel and Veronis 1960), resolving all the relevant length and times scales. Due to the use of the Boussinesq approximation, temperatures and densities are related by a linearized equation of state,

$$\rho = \rho_0 \left[1 - (T - T_0)/T_0\right]. \tag{1}$$

Following Kim et al. (1987), we take the curl of the momentum equations (twice) to recast them in the form of two evolution equations, one for the vertical component of the vorticity ($\omega_z = [\nabla \times \mathbf{u}]_z$), and one for the Laplacian of the vertical velocity ($\phi = \nabla^2 w = [\nabla \times \boldsymbol{\omega}]_z$),

$$\partial_t \phi + NL_\phi = \nu \nabla^2 \phi - g/\rho_0 (\partial_{xx} + \partial_{yy})\rho, \tag{2}$$

$$\partial_t \omega_z + NL_\omega = \nu \nabla^2 \omega_z, \tag{3}$$

where g is the acceleration due to gravity and ν is the kinematic viscosity. The non-linear terms are

$$NL_\phi = -(\partial_{xx} + \partial_{yy})H_3 + \partial_z \left(\partial_x H_1 + \partial_y H_2\right) \tag{4}$$

$$NL_\omega = \partial_y H_1 - \partial_x H_2, \tag{5}$$

where $\mathbf{H} = \mathbf{u} \times \boldsymbol{\omega}$ is the helicity.

While the fluctuating velocities can be obtained from the definitions of ϕ, ω_z and the continuity equation, the same is not true for the mean horizontal velocities, $U = \langle u \rangle$ and $V = \langle v \rangle$, where $\langle \cdot \rangle$ denotes a spatial average in horizontal planes. For that reason, evolution equations for U and V need to be solved in addition to Eqs. 2 and 3,

$$\partial_t U = u_*^2/h - \partial_z \langle uw \rangle + \nu \partial_{zz} U, \tag{6}$$

$$\partial_t V = -\partial_z \langle vw \rangle + \nu \partial_{zz} V. \tag{7}$$

Note that the continuity equation requires the mean velocity in the vertical direction to be zero. In Eq. 6 the constant pressure gradient driving the flow is expressed as u_*^2/h, where h is the height of the domain and u_* is the friction velocity. Note that this definition of the friction velocity differs from the friction velocity at the ground ($u_\tau^2 = \nu \partial_z U|_0$) when $\partial_t U \neq 0$.

The system given by Eqs. 2–7 is completed with the energy equation, which provides an evolution equation for the total density ρ, taken to be the density deviation from the constant density at the top boundary,

$$\partial_t \rho + u \partial_x \rho + v \partial_y \rho + w \partial_z \rho = k \nabla^2 \rho, \tag{8}$$

where k is the thermal diffusivity.

Formulations of the Navier-Stokes equations based on ϕ and ω_z have been widely used in the past for the simulation of incompressible turbulent flows (Kim et al. 1987; del Álamo et al. 2004; Flores and Jiménez 2006; Hoyas and Jiménez 2006). They offer the major advantage of not requiring an explicit calculation of the pressure. Pressure-projection algorithms are computationally expensive, requiring more memory and operations than the present formulation. For these reasons the latter is usually preferred for incompressible flows in simple geometries. This formulation has also been recently used by García-Villalba and del Álamo (2009) to simulate turbulent channels with stable stratification and isothermal walls.

The boundary condition imposed at the ground ($z = 0$) is zero velocity, with a constant (cooling) heat flux $(w\rho)_0$, that models the effect that the radiative cooling of the ground has on the overlying air. This heat flux is imposed by fixing the density gradient $\partial_z \rho$ at the ground, so that $(w\rho)_0 = -k \partial_z \rho_0$. The boundary condition at the top is constant density ($\rho = 0$) with a free-slip condition for the velocities.

The numerical code used here is an extension of that used by Flores and Jiménez (2006), with the addition of the energy equation (Eq. 8) and the buoyancy term in Eq. 2. The time discretization is based on a third-order Runge-Kutta with an implicit timestep for the viscous terms. Fourier expansions are used in the horizontal directions (dealiased using the 2/3 rule), and a fourth-order compact finite-difference scheme is used to compute derivatives in the vertical direction.

Table 1 Parameters of the simulations

		Re	Pr	h/L	Lu_*/ν	N	Tu_*/h	L_x, L_y	
—	M00	360	1.0	0.00	∞	1	13	$5h, 5h$	Neutral
•	M04	360	1.0	0.41	878	1	28	$5h, 5h$	Turbulent
■	M20	360	1.0	2.05	175	1	22	$5h, 5h$	Laminar
—	S00	560	1.0	0.00	∞	1	26	$2\pi h, \pi h$	Neutral
○	S04	560	1.0	0.41	1366	2	80	$2\pi h, \pi h$	Turbulent
◇	S05	560	1.0	0.51	1098	1	17	$2\pi h, \pi h$	Turbulent
□	S06	560	1.0	0.61	918	1	17	$2\pi h, \pi h$	Turbulent
△,▽	S08	560	1.0	0.82	683	3	98	$2\pi h, \pi h$	Turb/lam
+	S12	560	1.0	1.23	455	1	26	$2\pi h, \pi h$	Laminar
×	P12	560	0.5	1.23	455	1	10	$2\pi h, \pi h$	Laminar
+	S20	560	1.0	2.05	273	1	16	$2\pi h, \pi h$	Laminar
—	L00	560	1.0	0.00	∞	1	22	$8\pi h, 4\pi h$	Neutral
•	L04	560	1.0	0.41	1366	1	25	$8\pi h, 4\pi h$	Turbulent
▲	L08	560	1.0	0.82	683	1	63	$8\pi h, 4\pi h$	Turb/lam
▼	L10	560	1.0	1.03	544	1	15	$8\pi h, 4\pi h$	Laminar

N is the number of runs using different initial conditions considered in each case, and Tu_*/h is length of the longest time history available. For case S08, △ is used for the runs where the final state is turbulent, while ▽ is used for the cases where the final state is laminar

In the numerical code Eqs. 2–8 are cast in non-dimensional form, using h, u_* and $(w\rho)_0$ as characteristic scales. Hence, the flow is fully characterized by the Reynolds number $Re = u_* h/\nu$, the Prandtl number $Pr = \nu/k$, and the ratio of the Obukhov length to h,

$$L/h = \frac{u_*^3/(\kappa h)}{g/\rho_0 (w\rho)_0}. \tag{9}$$

As mentioned in the introduction, the Obukhov length provides the scale for the thickness of the dynamic sublayer, since it is defined as the height at which the buoyancy flux is of the same order as the turbulent energy production (Monin 1970).

Table 1 presents a summary of the conditions considered in the present paper. Two different Reynolds numbers, $Re = 360$ and $Re = 560$ are considered. The low Reynolds number cases (M00, M04 and M20) have the same computational domain as Nieuwstadt (2005) ($L_x \times L_y = 5h \times 5h$), and were chosen to verify the code. For $Re_\tau = 560$ we consider two computational domains, cases S00–S20 have $L_x \times L_y = 2\pi h \times \pi h$ and cases L00–L10 are $8\pi h \times 4\pi h$. In all of the above, $Pr = 1$. Only case P12 was run with $Pr = 0.5$, using a $2\pi h \times \pi h$ domain. The resolution of the grid is the same in all the runs; $\Delta_x^+ \lesssim 12$, $\Delta_y^+ \lesssim 6$ and $\Delta_z^+ \in [0.1, 6]$, where the $^+$ superscript indicates variables normalized using u_* and ν. The range of non-dimensional heat fluxes at the ground, h/L, was chosen to span the resulting types of flows, from those that remain turbulent to those that relaminarize.

The simulations are initialized as follows: for each Re and domain size, first we run a non-stratified case ($h/L = 0$) until it reaches a statistically steady state: cases S00, M00 and L00. Flow fields from those cases are used as initial conditions for the stratified cases, so that at the initial time $\rho = 0$ everywhere. This initialization is consistent with neutral conditions at sunset (Metzger et al. 2007), and is found in several simulations in the literature (Coleman et al. 1992; Nieuwstadt 2005; Van de Wiel et al. 2007; Edwards 2009). Finally, to assess the

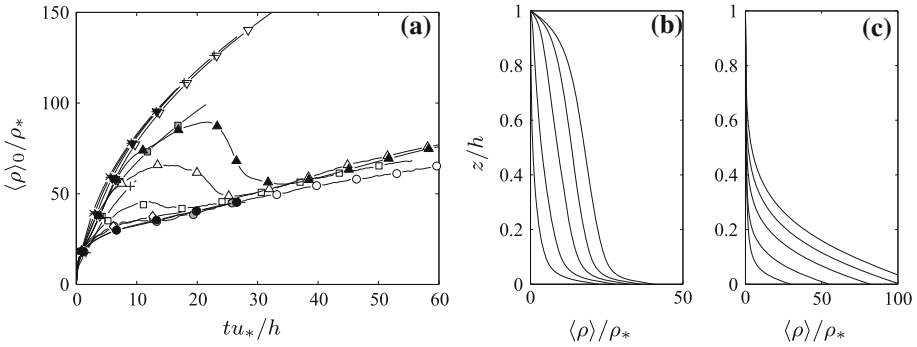

Fig. 1 **a** Time evolution of the mean density at the ground ($z = 0$). Symbols as in Table 1. **b** Vertical profiles of the mean density for a turbulent case, S04. Different lines correspond to times $tu_*/h = 2, 5, 10, 15, 20$, increasing from left to right. **c** Same as (**b**) but for a laminar case, S12

effect that a particular initial condition has on the evolution of the stratified cases, some cases have been run for different realizations of the initial non-stratified velocity fields (parameter N in Table 1).

3 Results

3.1 Overview of the Evolution of the Flow

As the cooling heat flux $(w\rho)_0$ is applied at the ground, a stable stratification develops in the channel. Depending on the magnitude of $(w\rho)_0$, the flow rapidly evolves towards a laminar state, or remains turbulent. Figure 1a shows the evolution of the mean density at the ground $\langle\rho\rangle(z = 0) = \langle\rho\rangle_0$, for the all the cases given in Table 1. The density is normalized with ρ_*, which is defined using the heat flux imposed at the ground and the friction velocity, $u_*\rho_* = (w\rho)_0$. At $t = 0$ the density is uniform everywhere. There is then an initial transient where most of the heat transfer is due to molecular diffusion, resulting in $\rho \propto \sqrt{th^2/k}$. After that initial transient, either the density at the wall grows roughly linearly with time for the cases where turbulence survives, or the turbulent fluctuations are suppressed and the $t^{1/2}$ behaviour continues (laminar cases).

Figure 1b, c shows the time evolution of vertical profiles of $\langle\rho\rangle$ for two typical cases, S04 as an example of a turbulent case and S12 as an example of a laminar case. We can observe that, at all times, the density profiles from case S04 resemble the weakly stable profiles described by Mahrt (1998), with a reasonably well-mixed region occupying most of the channel height. On the other hand, the density distribution of case S12 (Fig. 1c) resembles the very stable profiles of Mahrt (1998), where the absence of a mixed region indicates that the flow is laminar everywhere. Comparison of Fig. 1b, c shows that the absence of turbulent fluctuations in S12 yields much higher densities (lower temperatures) at the ground, both in dimensional and in non-dimensional form. Note that S04 and S12 have the same value of u_*, but S12 has a larger heat flux $(w\rho)_0$ (stronger stratification), implying that ρ_* is larger in S12 than in S04.

The behaviour of the mean velocity is consistent with the above description of the flow. Figure 2a shows the total mass flux $M = \int U dz$, normalized with its initial value, for the all the cases given in Table 1. Turbulent/weakly stable cases exhibit mass fluxes that vary slowly

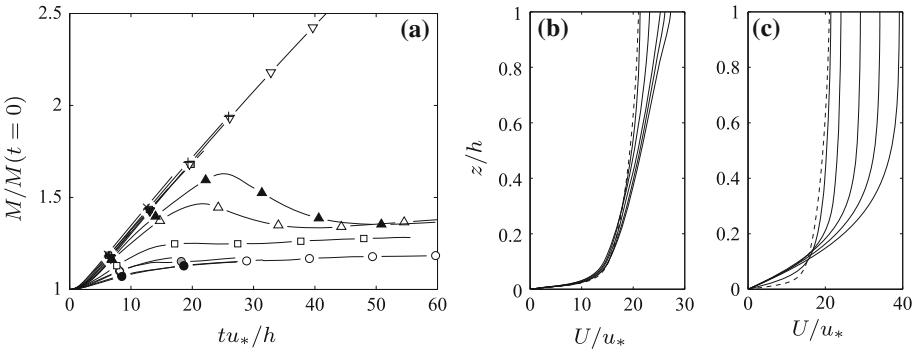

Fig. 2 **a** Time evolution of the total mass flux $M = \int U dz$. Symbols as in Table 1. **b** Vertical profiles of the mean streamwise velocity for a turbulent case, S04. Different lines correspond to times $tu_*/h = 2, 5, 10, 15, 20$, increasing from left to right. **c** Same as (**b**) but for a laminar case, S12. The *dashed line* in (**b**) and (**c**) correspond to the initial mean velocity profile, case S00

with time, while laminar/very stable cases show a rapid linear growth of the mass flux with time, as in Garg et al. (2000). We can observe in Fig. 2b that the slow increase of M for a turbulent case, S04, is due to the acceleration of the upper part of the channel ($z/h \gtrsim 0.5$), where the stabilizing effect of the stratification reduces the turbulent Reynolds stresses that are no longer able to compensate the streamwise pressure gradient driving the flow. Although not shown here, similar results are obtained for the other turbulent cases, M04, S05 and S06. In all of them, U shows the logarithmic plus linear profile predicted by the similarity theory (Monin 1970) in the lower half of the channel, with velocities close to those observed in the neutral case S00.

For the laminar/very stable cases, Fig. 2c shows how an initially turbulent profile evolves towards a laminar parabolic profile. U is reduced near the ground, and increases linearly everywhere else, consistent with the time evolution of M shown in Fig. 2a.

The vertical profiles of mean density and mean velocity shown in Figs. 1 and 2 agree well with those reported by Nieuwstadt (2005) at $Re = 360$.

3.2 Time Development of Turbulent Fluctuations

To analyze the decay and eventual collapse of the turbulence in more detail, we focus on the time evolution of the r.m.s. of the vertical velocity fluctuations $\sigma_w = \langle w^2 \rangle^{1/2}$. In the near-wall region (Fig. 3a), when the vertical velocity is normalized with u_*, all cases show the same initial decay for $tu_*/L \lesssim 10$. This suggests that the time needed by turbulent structures in the buffer region to reflect the change in the heat flux at the ground scales with L/u_*.

This result is consistent with an order of magnitude analysis of the evolution equation for the horizontal average of the energy contained in the vertical velocity, $\langle w^2 \rangle$. If we assume that, for short times, the buoyancy flux term is solely responsible for the time variation of $\langle w^2 \rangle$, we obtain

$$\partial_t \langle w^2 \rangle \approx g/\rho_0 \langle w\rho \rangle \rightarrow \frac{u_*^2}{t_c} \approx g/\rho_0 (w\rho)_0 \rightarrow t_c \approx \frac{u_*}{g/\rho_0 (w\rho)_0} = \frac{L}{u_*}. \tag{10}$$

The above expression assumes that σ_w scales with u_*, and the buoyancy flux $\langle w\rho \rangle$ scales with $(w\rho)_0$, the cooling flux imposed at the ground. The latter is corroborated by the vertical profiles of $\langle w\rho \rangle$ (not shown here).

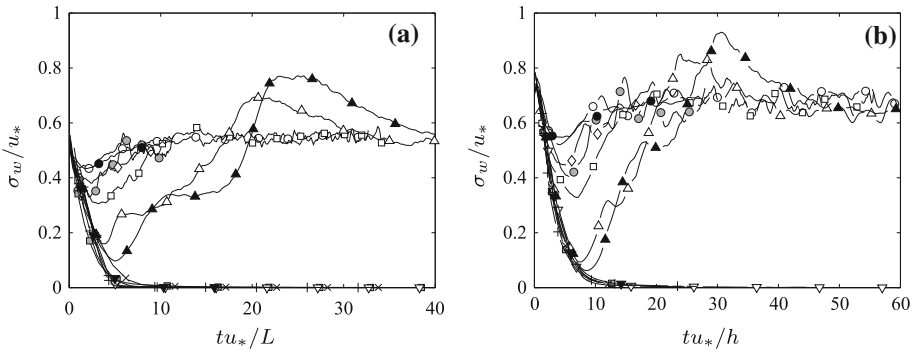

Fig. 3 Time evolution of the r.m.s. of the vertical velocity fluctuations at **a** $z^+ = zu_*/\nu = 15$ and **b** $z/h = 2/3$. Symbols as in Table 1

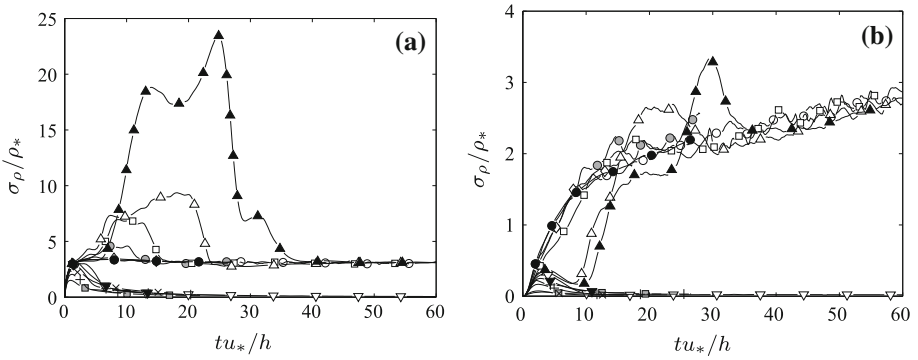

Fig. 4 Time evolution of the r.m.s. of the density fluctuations at **a** $z^+ = 15$ and **b** $z/h = 2/3$. Symbols as in Table 1

Interestingly, this time scaling does not hold during the adjustment of the flow in the outer region, defined as the region where $z \sim h$. At such distances from the ground the initial decay of the turbulent fluctuations occurs on a different time scale, h/u_*, as shown in Fig. 3b. Note that the ratio h/L varies from 0.2 to 2 for the cases presented in Fig. 3, so that a collapse in tu_*/h excludes a collapse in tu_*/L, and vice versa.

These results suggest that, while the imposed ground cooling has a direct effect on the buffer region near the ground, its effect in the outer region is felt as the density fluctuations generated near the ground are transported upwards by eddies with characteristic sizes and velocities of the order of h and u_*. Indeed, Fig. 4 shows that the time for the development of the buoyancy flux and the density fluctuations scales with h/u_*, both near the ground (Fig. 4a) and in the outer region (Fig. 4b). This scaling for the initial development of the density field is not surprising, since at $t = 0$ we have $\rho = 0$ everywhere, and the density field has to be driven by the pre-existing turbulent eddies in the channel.

As h/L increases beyond a critical value, σ_w and σ_ρ do not recover to levels similar to the non-stratified equilibrium values. The flow becomes laminar and σ_w and σ_ρ fall to zero. For cases S- and L- the threshold appears to be $(h/L)_{crit} \approx 0.82$. Indeed, out of the three realizations available for case S08, two evolve towards a turbulent state ($\triangle$) and one evolves towards a laminar state ($\triangledown$). Note also that this collapse of turbulence is related to the

magnitude of the buoyancy flux, and not to the strength of the density gradient at the ground. Figures 3 and 4 show that case P12 ($Pr = 0.5, h/L = 1.2$) relaminarizes as in case S12 ($Pr = 1, h/L = 1.2$), even if it has the same density gradient at the ground as case S06 ($Pr = 1, h/L = 0.6$, turbulent).

Plots similar to those presented in Fig. 3 are obtained for the other two velocity components, as well as for the Reynolds stresses and the turbulent transport terms (not shown). All of them level off at large times, suggesting that the flow reaches a quasi-steady state. However, Fig. 4 shows that the density fluctuations σ_ρ only level off near the ground. The most likely explanation for the increase of σ_ρ in the outer region is the continuous development of stronger mean density gradients in the upper part of the channel, as shown in Fig. 1b. This process continues until the heat flux at $z = h$ balances the heat flux imposed at the ground, and the system reaches a truly statistically steady state. None of the simulated cases has been run for such long times.

Another interesting feature of the time evolution of σ_ρ is the peak at $tu_*/h \gtrsim 10$ near the ground (Fig. 4a). The intensity of the peak increases with h/L, and it is maximum for case L08, which has $h/L = (h/L)_{crit}$. Figure 5 shows the time evolution of instantaneous isopycnals near the ground from that case, where we can observe that the evolution of the density field is very non-uniform in the horizontal plane. At $tu_*/h \approx 5$ we observe turbulent patches on an otherwise laminar low. At $tu_*/h \approx 8$ only one of the patches survives, and it grows in the streamwise direction until it covers the whole length of the computational domain by $tu_*/h \approx 10$. At those times, vertical profiles of mean density in the turbulent region are similar to those presented in Fig. 1b, while those in the laminar regions resemble those in Fig. 1c. The difference between the mean densities in the laminar and turbulent regions close to the ground is roughly $\Delta\rho \approx 15\rho_*$, which explains the secondary peak in Fig. 4a. At later times, $tu_*/h \gtrsim 40$, the flow becomes turbulent everywhere, and the horizontal intermittency disappears. This horizontal intermittency becomes weaker as smaller values of h/L are considered, with the consequent decrease in the intensity of the secondary peaks in σ_ρ. Similar secondary peaks are also observed in the velocity fluctuations shown in Fig. 3a, and they were also reported by Nieuwstadt (2005), who did not link them to horizontal intermittency. Also note that this horizontal intermittency is consistent with the global intermittency described by Mahrt (1998) for very stable cases, although in the present case it cannot be associated to top-down interactions.

It is important to note that the two-stripe configuration observed in Fig. 5c is most likely produced by the numerical domain not being large enough to accommodate the turbulent patch observed in Fig. 5b. Similar results have been recently reported by García-Villalba and del Álamo (2011) who note that, in the quasi-steady state of stratified turbulent channel flows with isothermal walls at comparable Re, domains as large as $8\pi \times 6\pi$ are needed to properly capture spatial intermittency.

The artificial character of Fig. 5c explains the differences in the time evolution of cases S08 and L08 (Figs. 3 and 4 in the time range $10 \lesssim tu_*/h \lesssim 50$). The recovery of the turbulence in the larger box takes longer than in the small box, even if they both have the same Re, Pr and h/L. This discrepancy between the large and small box cases is not observed for the weaker stratification of cases S04 and L04, suggesting that the transition in the latter is properly captured. Also note that the conclusions drawn from Fig. 3 and the critical character of cases with $h/L = 0.82$ are not affected by this limitation, since they are based on the behaviour of the flow before the development of the two-stripe configuration shown in 5c. Similar precautions will be taken in the following sections, namely to limit the conclusions to those based on the behaviour of L08 for $tu_*/h \lesssim 10$ and $tu_*/h \gtrsim 50$.

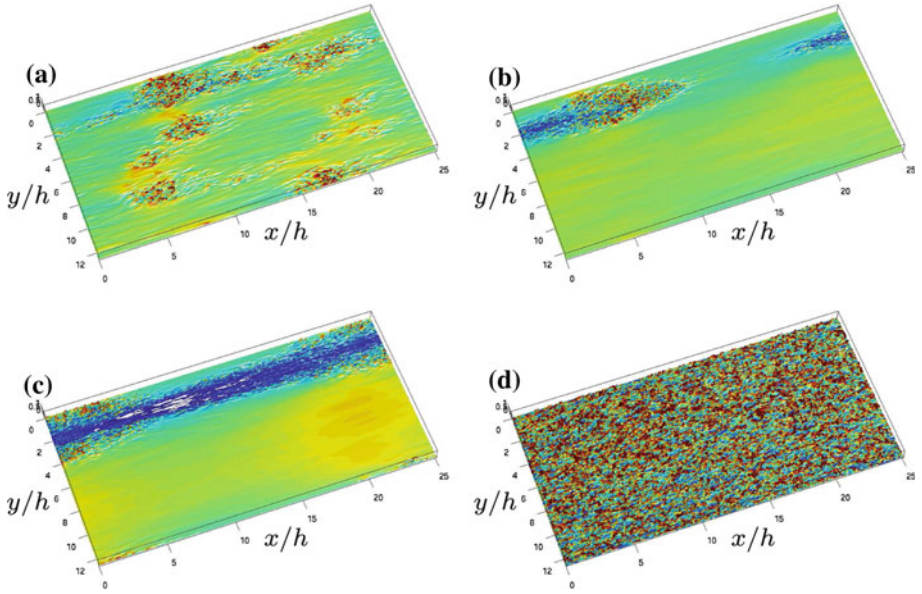

Fig. 5 Instantaneous isopycnals $\rho = \langle\rho\rangle(z = 0.1h)$, for case L08. **a** $tu_*/h = 5$, **b** $tu_*/h = 8$, **c** $tu_*/h = 10$, **d** $tu_*/h = 60$. The isopycnals are coloured with the distance to the ground, *blue* for $z = 0$ and *red* for $z \geq 0.2h$

3.3 Criterion for Turbulence Collapse

As discussed in the previous section, Fig. 3 shows that $(h/L)_{crit} = 0.82$ for $Re = 550$. This critical value differs from the value $h/L_{crit} = 0.51$ reported by Nieuwstadt (2005) in the same flow configuration, but with a smaller $Re = 360$. At even lower Reynolds numbers, $Re = 180$, the simulations by Garg et al. (2000) and Armenio and Sarkar (2002) of channels with isothermal walls suggest a critical value $(h/L)_{crit} \approx 0.24$. The differences in the values of $(h/L)_{crit}$ for different Reynolds numbers suggest that h/L is not an appropriate parameter to characterize the initial collapse of turbulence. However, when the critical value of the Obukhov length is normalized with the viscous length scale ν/u_*, the values of $Re_L = Lu_*/\nu$ are approximately 650 for channel flows with isothermal boundaries, 705 for Nieuwtadt's simulations, and 683 for the present simulations (case L08). This suggests that Re_L, the ratio between the Obukhov and the viscous length scale, is a better criterion than h/L to determine when turbulence collapses.

Figure 6a compares our simulations with laboratory boundary layers (Ohya et al. 1997; Ohya 2001) and ABL measurements. The latter are from the CASES-99 campaign, in which turbulent and radiative heat fluxes, friction velocities and boundary-layer height measurements (among others) were taken for 28 nights over dry, relatively flat open prairie grass ($k_r \lesssim 0.25$ m) in Kansas. Most of those nights had clear sky conditions, with little cloud cover. Full details of the experiment can be found in Poulos et al. (2002) and in http://www.colorado-research.com/cases/CASES-99.html.

The CASES-99 data used in Fig. 6 have been extracted from Van de Wiel et al. (2003), and they correspond to time averages over 0000-0600 LST. For the laboratory boundary layer, it is assumed that the height of the surface layer (h) is equal to the boundary-layer thickness, since rotation effects are not present in those experiments. For the ABL data, h is estimated using

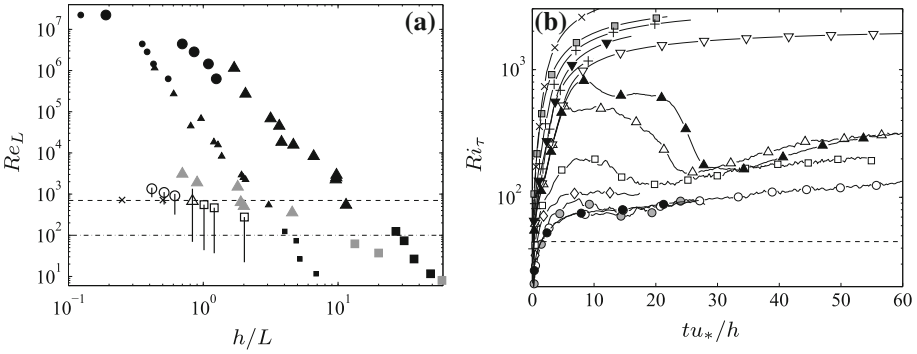

Fig. 6 **a** Comparison of DNS and experimental data. ○, turbulent cases; △, intermittent/transitional/critical; □, radiative/laminar. *Solid symbols* correspond to CASES-99. The height of the surface layer h is estimated using Eq. 11, with $U_G = U_{10}/0.7$ (*large symbols*) and $U_G = 10\ \mathrm{m\ s^{-1}}$ (*small symbols*). *Grey symbols* correspond to experimental boundary layers, Ohya et al. (1997) over a smooth surface, Ohya (2001) over a rough surface. *Open symbols* correspond to present DNS. The *vertical lines* show the range of values covered by Re_L during the time evolution of each case. The *crosses* mark the critical values found in Nieuwstadt (2005), Garg et al. (2000) and Armenio and Sarkar (2002). **b** Time evolution of Ri_τ, defined in Eq. 12. Symbols as in Table 1

$$h = a\frac{u_\tau^2}{fU_G}. \tag{11}$$

According to Monin (1970), Eq. 11 is an estimation of the thickness of the surface layer with an accuracy no lower than a percent. We use $f = 10^{-4}\ \mathrm{s^{-1}}$ for the Coriolis parameter, $a = 0.2$, and the geostrophic velocity U_G is estimated using $U_{10} = 0.7U_G$ (John Garratt, private communication, 2010), where U_{10} is the velocity measured at 10 m above the ground.

In their analysis of the CASES-99 data, Van de Wiel et al. (2003) identify three regimes, after discarding 8 of the 28 available nights: turbulent (40% of nights), intermittent or transitional (40%), and radiative (20%). While all nights show relatively large net radiative cooling (characteristic of clear skies), radiative nights have small turbulent heat fluxes ($\approx$1 W m^{-2}) compared to turbulent and intermittent nights ($\approx$10−30 W m^{-2}). This strongly suggests that, at least in the lower 2 m of the boundary layer where flux measurements are taken, the flow in the radiative nights could have been essentially laminar. Indeed, we observe in Fig. 6a that the limit in Re_L between intermittent (△) and radiative (□) nights roughly agrees with the limit in the DNS and laboratory boundary-layer data between turbulent and laminar cases.

Note that for our DNS, Re_L is the ratio between the Obukhov and viscous length scales at time $t = 0$. As the stratified open channel flows evolve in time, the instantaneous friction velocity at the wall $u_\tau = (\nu\partial_z U|_0)^{1/2}$ varies with time. We can take that effect into account using u_τ instead of u_* in the definitions of L (Eq. 9) and Re_L. The range of values covered by the 'instantaneous' Re_L is indicated by the vertical lines in Fig. 6a, and suggests that the open channel flow relaminarizes if the value of Re_L during its evolution falls below $Re_{L,crit} \approx 100$. Figure 6a shows that this critical value appears to be in better agreement with the laboratory and field data. It is important to note that the agreement in Re_L between DNS, laboratory and field data is independent of the details of the definition of h. For instance, the small symbols in Fig. 6a have $U_G = 10\ \mathrm{m\ s^{-1}}$ instead of $U_G = U_{10}/0.7$, which yields a horizontal displacement of the experimental points. A similar effect is observed when the value of a in Eq. 11 is changed.

As mentioned in the introduction, the thickness of the dynamic sublayer is proportional to the Obukhov length, L, and the height of the buffer region is $\approx 100\nu/u_\tau$. Therefore, $Re_L = Lu_\tau/\nu < 100$ implies that the dynamic sublayer is not large enough to accommodate a buffer region. In other words, turbulence collapse occurs when there is insufficient scale separation between the largest $O(L)$ and smallest $O(\nu/u_\tau)$ scales of the dynamic sublayer to sustain continuous turbulent motions. Indeed, DNS of turbulent channel flows without stratification also show that the minimum height above which velocity fluctuations can be artificially damped without relaminarization of the underlying flow is $zu_\tau/\nu \approx 50-80$ (Jiménez and Simens 2001), in reasonable agreement with $Re_{L,crit} \approx 100$.

Two remarks should be made regarding the agreement between our DNS and CASES-99 data in Fig. 6. First, as mentioned in the introduction, our DNS neglects many physical processes occurring in the ABL, i.e. low-level jets and turbulence generated within them. In that sense, Fig. 6a seems to suggest that the collapse of turbulence near the ground is a local process, somewhat independent of the conditions of the ABL at higher altitudes. Interestingly, Fritts et al. (2003) report that during the night of 14 October 1999 (one of the radiative nights in Van de Wiel et al. 2003) the mean state was characterized by a low-level jet with maximum velocities of $\approx 8-12$ m s^{-1} at altitudes of $\approx 50-300$ m. This suggests that the presence of low-level jets does not prevent the collapse of turbulence in the dynamic sublayer, although more work is needed to clarify this point.

Second, the ground at CASES-99 is almost certainly rough. However, its roughness Reynolds number $k_r^+ = k_r u_\tau/\nu$ is relatively small for the radiative nights, $k_r^+ \lesssim 200$, especially compared to the values of the turbulent nights, $k_r^+ \gtrsim 2 \times 10^3$. This parameter is even smaller for the laboratory boundary layers of Ohya (2001) over rough surfaces, where $k_r^+ = 10-20$, indicating that these boundary layers are clearly transitionally rough (Raupach et al. 1991). Small values of k_r^+ would explain why smooth ground arguments seem to apply to flows over rough surfaces, as shown in Fig. 6.

The argument leading to $Re_L < 100$ as a criterion for turbulence collapse over smooth surfaces can be extended to rough surfaces. In that case, the roughness sublayer, whose height scales with k_r (Raupach et al. 1991), is substituted for the buffer region. The minimum scale separation argument proposed above then implies that the parameter that predicts turbulence collapse for a stable boundary layer over a rough surface is L/k_r, with a critical value $(L/k_r)_{crit} \sim 1$. CASES-99 data are consistent with this argument, since the transition between intermittent and radiative cases in that database occurs at $L/k_r \approx 0.5$. Note that this implies that, for CASES-99 data, both criteria ($Lu_\tau/\nu < 100$ and $L/k_r < 1$) are satisfied on radiative nights. At this time, and with the data available to us, it seems that it is an unfortunate coincidence, since in the transitionally rough data of Ohya (2001) turbulence collapse occurs at $Lu_\tau/\nu \sim 100$ and $L/k_r \sim 100$.

Finally, from Fig. 6a, little can be said about a criterion for distinguishing intermittent and continuously turbulent cases, other than $h/L \sim 1$ provides a very rough estimate for that limit.

3.3.1 Ri_τ versus Re_L

In order to finalize this section, we need to address the relationship between Ri_τ and Re_L. The question is whether Ri_τ is an appropriate criterion to describe turbulence collapse.

In channels with isothermal walls, the friction Richardson number is defined as $Ri_\tau = \Delta\rho g h/\rho_0 u_\tau^2$, where h is the channel half-height and $\Delta\rho$ is the density difference between the two walls. In our open channel simulations, the density at the ground varies with time,

and therefore so does Ri_τ. Assuming that the height of the open channels is equivalent to the half-height of the full channels, we take $\Delta\rho = 2\langle\rho\rangle_0$. This is a reasonable approximation, as can be confirmed by comparing the density profiles in Fig. 1 with the density profiles shown in Armenio and Sarkar (2002) and García-Villalba and del Álamo (2009).

Figure 6b shows the time evolution of Ri_τ for the present cases. The horizontal dashed line in the figure corresponds to $Ri_\tau = 45$, the critical value proposed by Garg et al. (2000) at $Re = 180$. All the cases in Table 1 are well above that value, and the maximum value of Ri_τ achieved by S08 and L08 (the critical cases) is $Ri_\tau \approx 10^3$, larger than the values observed in Garg et al. (2000) and Armenio and Sarkar (2002). This suggests that the critical Ri_τ depends on Re. Indeed, it is possible to show that Ri_τ and h/L are equivalent criteria, since

$$Ri_\tau \approx \frac{2}{\kappa}\frac{\langle\rho\rangle_0}{\rho_*}\left(\frac{h}{L}\right). \tag{12}$$

Therefore, the same Reynolds number dependency observed in h/L is present in Ri_τ. This Re dependency is also reported by García-Villalba and del Álamo (2011), who observe turbulent flow with laminar patches when $Ri_\tau \gtrsim 2 \times 10^3$ at $Re = 550$, in good agreement with our results. As noted by García-Villalba and del Álamo (2011), this critical Ri_τ value is much smaller than the linear stability limit, which is $Ri_\tau \sim 10^4$ for $Re_\tau \approx 550$ (Gage and Reid 1968). Indeed, all the laminar cases in Table 1 have asymptotic values of the friction Richardson number

$$Ri_{\tau,l} = \frac{2}{\kappa} Re\, Pr \left(\frac{h}{L}\right) \tag{13}$$

well below the linear stability limit (for the most stratified case, L20, $Ri_{\tau,l} = 5 \times 10^3 < 10^4$). Therefore, as the mean velocity in the laminar cases evolves towards a parabolic laminar profile, they should become unstable again. None of our cases has been run for times long enough to observe this behaviour.

3.4 Effect of the Coherent Scales of the Outer Region

We have seen in Sect. 3.2 that the density field initially develops on times $t \sim h/u_*$ of the same order as the turnover times of the large-scale eddies in the pre-existing turbulent flow. These structures might have an important role on the process of turbulence collapse, which is also suggested by the presence of turbulent patches with sizes O(h) in the instantaneous visualizations shown in Fig. 5. Indeed, out of the three realizations of case S08, the one that evolves towards a laminar state has an initial condition with slightly lower turbulent kinetic energy in the outer region (5% less than the average).

For non-stratified turbulent channel flows, it has been long known that the most common structures of the outer region ($z \sim h$) are very long, streamwise velocity structures over both smooth (Kim and Adrian 1999; del Álamo et al. 2004; Hutchins and Marusic 2007) and rough surfaces (Flores and Jiménez 2006). These structures are alternating streaks of high and low velocity, with characteristic velocities of the order of u_*, heights and widths of the order of the thickness of the flow h, and streamwise lengths $l_x \gtrsim 20h$. They were termed global modes by del Álamo et al. (2004), because they are correlated across the whole flow thickness. They mix momentum across the whole flow thickness, raising turbulence from the wall in the low-velocity regions, and compressing the mean velocity profile towards the wall in the high-speed regions. Indeed, del Álamo and Jiménez (2003) and Hoyas and Jiménez (2006) showed that the global modes have strong spectral signatures in the

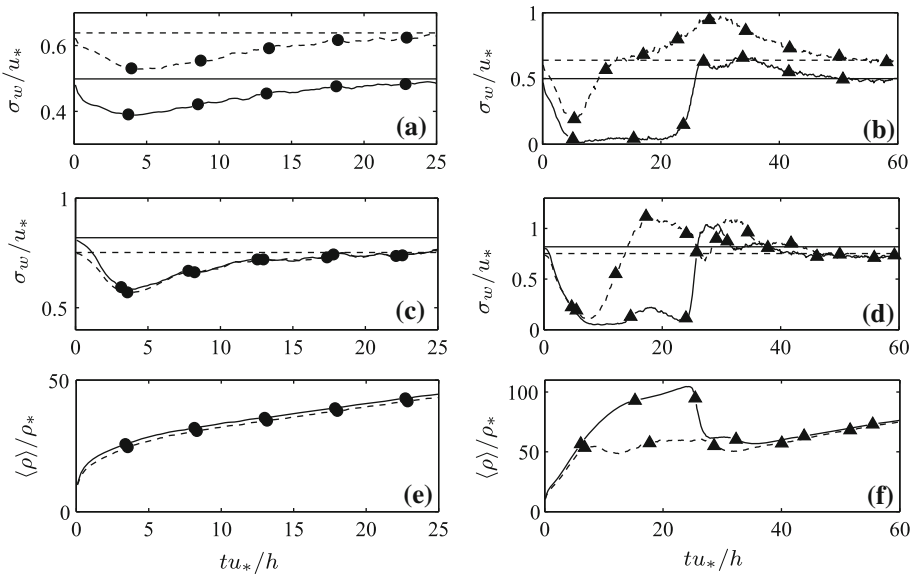

Fig. 7 Time history of vertical r.m.s. velocity at $zu_*/\nu = 15$ (**a**, **b**), $z/h = 2/3$ (**c**, **d**) and density at the ground (**e**, **f**) for cases L04 (**a**, **c**, **e**) and L08 (**b**, **d**, **f**). ——, low shear regions. - - - -, high shear regions. The *horizontal lines* correspond to the mean value of the non-stratified case L00

streamwise velocity component near the ground at streamwise and spanwise wavelengths $\lambda_x \approx 10h$ and $\lambda_y \approx 1.5h$.

We analyze the effect that those structures have on the process of turbulence collapse by computing one-point statistics, conditioned on horizontal areas where the local shear stresses at the ground $\tau_L(x, y, t)$ are larger or smaller than the horizontal average, $\langle\tau\rangle(t)$. Low-shear regions ($\tau_L < \langle\tau\rangle$) are associated with regions of low streamwise velocity and upward vertical velocity, while high-shear regions are associated with high streamwise velocities and mainly downward vertical motions (Mathis et al. 2009).

In order to remove the effect of the near-wall streaks, we define the local shear stresses at the ground τ_L as a box-average of the instantaneous shear stresses $\tau(x, y, t)$,

$$\tau_L(x, y, t) = \frac{1}{l_x l_y} \int_{-l_x/2}^{lx/2} \int_{-l_y/2}^{l_y/2} \tau(\xi + x, \eta + y, t) d\xi d\eta. \tag{14}$$

The results presented here have $l_x = h/2$, $l_y = h/2$, but similar results are obtained provided that the averaging box is larger than the near-wall streaks, $l_x, l_y > 100\nu/u_*$.

Figure 7a, b shows that, in the buffer region, stratified and non-stratified cases have higher turbulent intensities within the high-shear regions than within the low-shear regions, in agreement with Mathis et al. (2009). Figure 7b shows that, for the critical case L08, the low-momentum regions relaminarize around $tu_*/h \sim 5$, while the high-shear regions remain turbulent. This is consistent with Fig. 5a and implies that, during the initial transient, the turbulent patches correspond to the high velocity global modes, and the laminar regions correspond to the low velocity global modes.

Figure 7c, d shows that in the outer region of non-stratified simulations (horizontal lines) the low-shear regions are more energetic than the high-shear regions. This should be expected

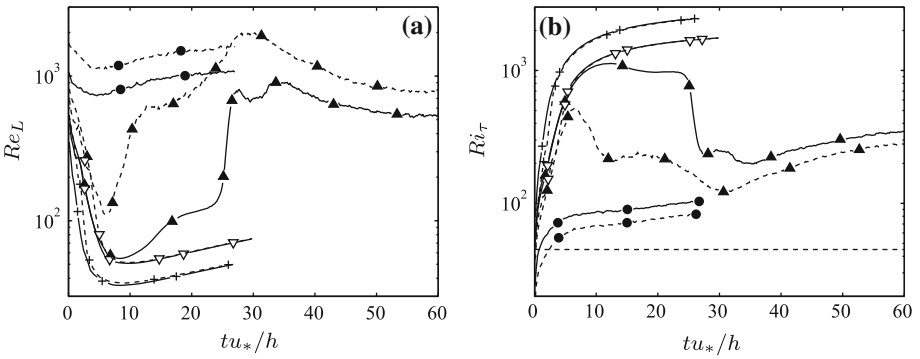

Fig. 8 Time evolution of **a** Re_L and **b** Ri_τ, when defined using the locally-averaged friction velocity $u^2_{\tau,L} = \tau_L$. Symbols as in Table 1. ——, low-shear regions. - - - -, high-shear regions.

since low-shear regions correspond to upward vertical motions that transport turbulent kinetic energy from the ground into the outer region. In the high-shear regions, the vertical motions are mainly downward, resulting in lower turbulent intensities.

The stratified cases show the same behaviour as the non-stratified case for $tu_*/h \lesssim 2$. However, for $tu_*/h > 2$, the vertical velocity fluctuations become independent of the shear at the wall, both in L04 (Fig. 7c) and L08 (Fig. 7d). This suggests that the stable stratification is damping the vertical motions associated to the global modes, resulting in a homogenization of σ_w. At $tu_*/h \approx 5$, case L08 has little energy in σ_w, but the turbulent motions growing near the ground in the high shear regions (Fig. 7b) reach the outer region and keep those regions of the flow active. For longer times, once the flow reaches a quasi-steady state, case L08 behaves as case L04, with σ_w being independent of the local shear at the ground. This quasi-steady behaviour is consistent with a z-less stratification (Nieuwstadt and Duynkerke 1996).

Figure 7e, f shows the evolution of the density at the ground. While for case L04 the high and low shear regions have very similar densities, the same is not true for case L08. In the low shear regions, the laminarization of the flow results in higher densities (lower temperatures), while in the turbulent regions the presence of a turbulent heat flux heating the ground from above allows lower densities (higher temperatures). The evolution of $\langle\rho\rangle_0$ inside the low-shear regions is consistent with the "runaway cooling" reported by Derbyshire (1999) and Van de Wiel et al. (2007). However, as noted in the introduction, the effects of radiative cooling of the air are not included in this simulation, and these might play an important role in reducing those density (temperature) differences.

Since case L08 suggests that both laminar and turbulent regions can coexist under certain conditions, it would be desirable to develop a criterion similar to the one proposed in Sect. 6, but based on local variables. To that purpose, we redefine L and Re_L using the locally averaged friction velocity $u^2_{\tau,L} = \tau_L$. Figure 8a shows the time history of Re_L computed over high- and low-shear regions, for cases L04, L08, S08 and S12. We observe that the minimum value of Re_L in the regions that remain turbulent (high shear) is $O(10^2)$, and comparison of Fig. 8a with Fig. 7b shows that the low-shear regions of case L08 stay laminar while their local $Re_L \lesssim 100$. This suggests that the criterion discussed in Sect. 3.3 can be used locally to predict collapse of the turbulence in a small region of the flow.

Finally, to complete the discussion presented in Sect. 3.3.1, Fig. 8b shows the time evolution of the local friction Richardson number, based on the local shear and the local density at

the wall. The results are similar to the Ri_τ evolution shown in Fig. 6b, with a slightly smaller value of the critical Richardson number, $Ri_\tau \approx 500$. Note that this value is still much larger than the critical value given by Garg et al. (2000), supporting the Re-number dependency of the Ri_τ-based criterion for turbulence collapse.

4 Conclusions

We have performed DNS of open channel flows with stable stratification, which can be used as a simple model for the surface layer of the ABL. A range of values of the cooling heat flux at the ground has been considered, yielding mean density profiles resembling the weakly stable and very stable cases distinguish by Mahrt (1998). While the former correspond to turbulent flows, the latter correspond to essentially laminar flows.

We have shown that for turbulent flows over smooth surfaces, the critical parameter that controls the transient relaminarization of the flow (collapse of turbulence) is $Re_L = Lu_\tau/\nu$, where L and u_τ are the local values of the Obukhov length and friction velocity. The critical value at which the local collapse of turbulence occurs is $Re_{L,crit} = (Lu_\tau/\nu)_{crit} \approx 100$, which is in good agreement with the lowest Re reported in non-stratified turbulent channel flows. This suggests that turbulence collapse is related to a lack of scale separation between the largest (O(L)) and smallest (O(ν/u_τ)) scales of the dynamic sublayer. When this argument is extended to rough surfaces, we obtain $(L/k_r)_{crit} \approx 1$, a threshold consistent with observations from the CASES-99 campaign.

Comparison of our DNS results with field data suggests that this collapse of the turbulence can also happen in the surface layer of the ABL when the mechanical forcing of the surface layer is very small ($U_{10} \approx 2$ m s^{-1} and $u_\tau \approx 0.02$ m s^{-1}). Under those conditions, the thickness of the surface layer is $h \sim 1$ m. Note that a laminar dynamic sublayer does not necessarily imply a laminar surface layer in the real ABL, in which top-down interactions can occur. Large-scale turbulent structures can be generated by the inflectional instability of the Ekman layer above the surface layer, and small-scale turbulence can be generated at the shear layers of the low-level jet, or by the breaking of internal waves.

Note that our results suggest that DNS or laboratory experiments at relatively low values of Re can be used to investigate local processes in the dynamic sublayer of the higher Re ABL, such as the collapse of ground shear-generated turbulence. This is possible provided that the relevant non-dimensional parameters (Lu_τ/ν for smooth surfaces, L/k_r for rough surfaces) are matched in the DNS or laboratory experiment.

Analysis of the decay of the turbulent fluctuations in the present DNS channel flow shows that, while the adjustment to the new heat flux occurs near the ground on times of the order of L/u_*, the adjustment in the outer region occurs in times of the order of h/u_*. This latter time is of the order of the eddy turnover time of the large scales in the non-stratified turbulent channel flow used as the initial condition. This suggests that these pre-existing large-scale turbulent motions have a critical impact on the development of the density field in the DNS. Indeed, our results indicate that, for the critical case in which turbulent and laminar regions co-exist during some time period, the turbulent regions of the flow correspond to the high-shear/high-velocity global modes identified in non-stratified wall-bounded turbulent flows. In the low-shear/low-velocity regions turbulence intensities are lower, and the ground temperatures are correspondingly lower, a phenomenon previously observed in RANS simulations. Similar effects can be expected in the ABL, since it also develops very long structures similar to the global modes during the neutral period around sunset (Metzger et al. 2007; Hutchins and Marusic 2007).

Acknowledgments This work has been supported by ARO Grant No. W911NF-08-1-0155. The numerical resources provided by Teragrid and the DoD HPCMP are gratefully acknowledged. We also appreciate fruitful discussions with J. C. del Álamo and M. García-Villalba, as well as the comments and suggestions of the reviewers.

References

Armenio V, Sarkar S (2002) An investigation of stably stratified turbulent channel flow using large-eddy simulation. J Fluid Mech 459:1–42

Beare RJ, Macvean MK, Holtslag AAM, Cuxart J, Esau I, Golaz JC, Jiménez MA, Khairoutdinov M, Kosovic B, Lewellen D, Lund TS, Lundquist JK, Mccabe A, Moene AF, Noh Y, Raasch S, Sullivan P (2006) An intercomparison of large-eddy simulations of the stable boundary layer. Boundary-Layer Meteorol 118(2):247–272

Coleman GN, Ferziger J, Spalart PR (1992) Direct simulation of the stably stratified turbulent Ekman layer. J Fluid Mech 244:677–712

Cuxart J, Jiménez M (2007) Mixing processes in a nocturnal low-level jet: an LES study. J Atmos Sci 64(5):1666–1679

del Álamo JC, Jiménez J (2003) Spectra of the very large anisotropic scales in turbulent channels. Phys Fluids 15(6):L41–L44

del Álamo JC, Jiménez J, Zandonade P, Moser R (2004) Scaling of the energy spectra of turbulent channels. J Fluid Mech 500:135–144

Derbyshire S (1999) Boundary-layer decoupling over cold surfaces as a physical boundary-instability. Boundary-Layer Meteorol 90(2):297–325

Edwards J (2009) Radiative processes in the stable boundary layer: part II. The development of the nocturnal boundary layer. Boundary-Layer Meteorol 131(2):127–146

Flores O, Jiménez J (2006) Effect of wall-boundary disturbances on turbulent channel flows. J Fluid Mech 566:357–376

Flores O, Jiménez J, del Álamo J (2007) Vorticity organization in the outer layer of turbulent channels with disturbed walls. J Fluid Mech 591:145–154

Fritts D, Nappo C, Riggin D, Balsley B, Eichinger W, Newsom R (2003) Analysis of ducted motions in the stable nocturnal boundary layer during CASES-99. J Atmos Sci 60(20):2450–2472

Gage K, Reid W (1968) Stability of thermally stratified plane Poiseuille flow. J Fluid Mech 33:21

García-Villalba M, del Álamo JC (2009) Turbulence and internal waves in a stably-stratified channel flow. In: High performance computing in science and engineering '08, vol 5. Springer, Berlin, pp 217–227

García-Villalba M, del Álamo JC (2011) Turbulence modification by stable stratification in channel flow. Phys Fluids (submitted)

Garg R, Ferziger J, Monismith S, Koseff J (2000) Stably stratified turbulent channel flows. I. Stratification regimes and turbulence suppression mechanism. Phys Fluids 12(10):2569–2594

Hogstrom U (1996) Review of some basic characteristics of the atmospheric surface layer. Boundary-Layer Meteorol 78(3–4):215–246

Hoyas S, Jiménez J (2006) Scaling of the velocity fluctuations in turbulent channels up to Re = 2003. Phys Fluids 18:011702

Hutchins N, Marusic I (2007) Evidence of very long meandering features in the logarithmic region of turbulent boundary layers. J Fluid Mech 579:1–28

Jiménez J, Simens MP (2001) Low-dimensional dynamics of a turbulent wall flow. J Fluid Mech 435:81–91

Kim K, Adrian RJ (1999) Very large-scale motion in the outer layer. Phys Fluids 11(2):417–422

Kim J, Moin P, Moser R (1987) Turbulence statistics in fully-developed channel flow at low Reynolds-number. J Fluid Mech 177:133–166

Kosovic B, Curry J (2000) A large eddy simulation study of a quasi-steady, stably stratified atmospheric boundary layer. J Atmos Sci 57(8):1052–1068

Mahrt L (1998) Stratified atmospheric boundary layers and breakdown of models. J Theor Comput Fluid Dyn 11(3–4):263–279

Mathis R, Hutchins N, Marusic I (2009) Large-scale amplitude modulation of the small-scale structures in turbulent boundary layers. J Fluid Mech 628:311–337

Metzger M, McKeon BJ, Holmes H (2007) The near-neutral atmospheric surface layer: turbulence and non-stationarity. Philos Trans R Soc A 365:859–876

Monin A (1970) Atmospheric boundary layer. Annu Rev Fluid Mech 2:225

Nieuwstadt F (2005) Direct numerical simulation of stable channel flow at large stability. Boundary-Layer Meteorol 116(2):277–299

Nieuwstadt F, Duynkerke P (1996) Turbulence in the atmospheric boundary layer. Atmos Res 40(2–4): 111–142

Ohya Y (2001) Wind-tunnel study of atmospheric stable boundary layers over a rough surface. Boundary-Layer Meteorol 98(1):57–82

Ohya Y, Neff D, Meroney R (1997) Turbulence structure in a stratified boundary layer under stable conditions. Boundary-Layer Meteorol 83(1):139–161

Pope SB (2000) Turbulent flows. Cambridge University Press, UK 264–290

Poulos G, Blumen W, Fritts D, Lundquist J, Sun J, Burns S, Nappo C, Banta R, Newsom R, Cuxart J, Terradellas E, Balsley B, Jensen M (2002) CASES-99: A comprehensive investigation of the stable nocturnal boundary layer. Bull Am Meteorol Soc 83(4):555–581

Raupach MR, Antonia RA, Rajagopalan S (1991) Rough-wall turbulent boundary layers. App Mech Rev 44:1–25

Saiki E, Moeng C, Sullivan P (2000) Large-eddy simulation of the stably stratified planetary boundary layer. Boundary-Layer Meteorol 95(1):1–30

Spiegel E, Veronis G (1960) On the Boussinesq approximation for a compressible fluid. J Astrophys 131(2):442–447

Stoll R, Porte-Agel F (2008) Large-eddy simulation of the stable atmospheric boundary layer using dynamic models with different averaging schemes. Boundary-Layer Meteorol 126(1):1–28

Sun J (1999) Diurnal variations of thermal roughness height over a grassland. Boundary-Layer Meteorol 92(3):407–427

Van de Wiel B, Moene A, Hartogensis O, De Bruin H, Holtslag A (2003) Intermittent turbulence in the stable boundary layer over land. Part II: A classification for observations during CASES-99. J Atmos Sci 60(20):2509–2522

Van de Wiel B, Moene A, Steeneveld G, Hartogensis O, Holtslag A (2007) Predicting the collapse of turbulence in stably stratified boundary layers. Flow Turbul Combust 79(3):251–274